ADVANCED ENERGY MATERIALS
www.advenergymat.de

Decoupling Membrane Electrode Assembly Materials Complexity from Fuel Cell Performance through Image-Based Multiphase and Multiphysics Modelling

Jianuo Chen, Wenjia Du, Zunmin Guo, Xuekun Lu, Matthew P. Tudball, Xiaochen Yang, Zeyu Zhou, Shangwei Zhou, Alexander Rack, Bratislav Lukic, Paul R. Shearing, Sarah J. Haigh, Stuart M. Holmes, and Thomas S. Miller**

Proton exchange membrane fuel cells (PEMFCs) are important clean energy technology, yet the material and structural complexity of their membrane electrode assemblies (MEAs) can hamper the development of next-generation structures, as even a subtle change to one component can have a significant impact on others. Mathematical modelling of PEMFC MEAs proves to be one of the few techniques able to decouple this complexity, but the available models are commonly based on over-simplified structures meaning they are less able to inform material design. In this study, an advanced image-based modelling approach is developed to reveal the interplay of material changes in PEMFC MEAs. Using high-temperature PEMFCs as an example system, advanced structural imaging techniques are used to produce a detailed 3D MEA reconstruction which forms the basis for the multiphase and multi-physics model. This allows both the prediction of cell performance and the decoupling the impact of changes to individual structures or components (such as membrane pores, catalyst cracks, and phase migration), on cell behaviour. These phenomena can then be selectively 're-coupled' to deconvolute the interplay of different materials employed within operational cells. The resulting insights provide a mechanistic understanding of MEA performance, guiding the design and optimisation of future PEMFCs.

1. Introduction

The ultimate efficiency and durability of proton exchange membrane fuel cells (PEMFCs), a critical clean energy technology, is driven by an array of complex interactions across multiple phases and physical fields, making cross-component synergy crucial.[1–3] Hence the materials within the membrane electrode assembly (MEA), which includes those used withi the membrane, catalysts, binders, ionomers, and gas diffusion media, should ideally be explored and developed as a unified system, rather than optimising them on a component-by-component basis.[4,5] Unfortunately, this is rarely possible due to the large number of separate components,[6] the complexity of the resulting parameter space,[7] interdependent behaviours,[8] diverse operational conditions, material degradation and manufacturing variability.[9] Achieving effective coordination among these

J. Chen, M. P. Tudball, S. Zhou, T. S. Miller
Electrochemical Innovation Lab
Department of Chemical Engineering
University College London
London WC1E 7JE, UK
E-mail: jianuo.chen@ucl.ac.uk; t.miller@ucl.ac.uk

J. Chen, Z. Guo, X. Yang, Z. Zhou, S. M. Holmes
Department of Chemical Engineering
University of Manchester
Oxford Road, Manchester M13 9PL, UK

The ORCID identification number(s) for the author(s) of this article can be found under https://doi.org/10.1002/aenm.202405179

DOI: 10.1002/aenm.202405179

W. Du, X. Lu, P. R. Shearing, T. S. Miller
The Faraday Institution, Quad One
Harwell Science and Innovation Campus
Didcot OX11 0RA, UK

W. Du, P. R. Shearing
Department of Engineering Science
University of Oxford
Oxford OX1 3PJ, UK

Z. Guo
Department of Mechanical and Industrial Engineering
University of Toronto
5 King's College Road, Toronto, Ontario M5S 3G8, Canada

X. Lu
School of Engineering and Materials Science
Queen Mary University of London
London, UK

components is essential for optimum fuel cell performance and durability, properties that must be maximised to enable further industrial application of PEMFCs.

The performance of catalysts in fuel cells is influenced by various factors, including catalytic activity, electrochemical surface area (ECSA), oxygen reduction reaction selectivity, support material properties, as well as particle size and distribution.[10,11] Simultaneously, the performance of fuel cell membranes is influenced by parameters such as proton conductivity, mechanical strength, chemical stability, gas permeability, water uptake, and thickness.[12,13] Yet, while fuel cell catalyst or membrane performance, for example, can be enhanced through approaches such as novel material synthesis,[12] modification,[14] doping,[15,16] grafting,[17] and cross-linking,[18] it is common for these improvements in individual component properties to have little impact on overall fuel cell performance. For instance, using graphene as catalyst support can increase ECSA, but the 2D nature of graphene can impede gas transport, thereby increasing mass transfer resistance[19,20] and negating any benefits. Similarly, while polyvinylpyrrolidone-polyethersulfone (PVP-PES) is a novel proton exchange membrane with excellent proton conductivity, its poor mechanical strength and solubility in water generated by the fuel cell can lead to significant hydrogen crossover, ultimately reducing cell performance.[21,22]

The impact of new materials or material modifications on PEMFC performance is often analysed using polarisation curves, electrochemical impedance spectroscopy (EIS), or various mathematical models.[23–25] Yet simulations of PEMFC MEAs often focus on single components, such as the gas diffusion layer (GDL) or catalyst layer (CL), using single-physics models that do not incorporate electrochemical reactions (primarily fluid dynamics simulations).[26–29] Simulations that combine electrochemical processes with multi-physics and multiphase coupling for the entire MEA are typically based on 2D models or simplified 3D models.[30–32] Single-component simulations, even if multi-physics, often struggle to account for interactions between components and between electrochemical reactions and physical changes. Similarly, 2D or simplified 3D models may fail to capture effects resulting from changes in the 3D structural morphology. Comprehensive multi-physics and multiphase coupling simulations based on detailed 3D models are relatively rare as the distribution and morphology of liquid water in real-world MEAs are challenging to capture, yet they have a significant impact on performance.

X-ray computed tomography (CT) is an excellent tool for reconstructing the structure of complex material systems.[33–36] However, the insensitivity of X-rays to light elements including water severely limits the achievable resolution when studying fuel cell MEAs. While neutron CT can visualize water distribution within PEMFCs, its spatial resolution is even more limited than X-ray CT.[37] Therefore, neutron CT is primarily utilized for analysing water distribution within the flow channels of the bipolar plates.[38] However, high-temperature proton exchange membrane fuel cells (HT-PEMFCs) often use phosphoric acid (PA)-doped membranes, enabling operation in the temperature range of 120–220 °C without relying on hydration. Due to its high boiling point, PA substitutes for water in HT-PEMFCs, eliminating the need for water management. Importantly, the relatively higher atomic mass of PA (compared to water), enhances the X-ray absorption coefficient of this material, making PA detectable. As PA leaches out of the membrane into the wider MEA microstructure, X-ray CT data can provide accurate 3D reconstructions of these vital components in the PEMFC's MEA.[34,39–42]

Our work leverages tomographic data from both focused ion beam-scanning electron microscopy (FIB-SEM) and micro X-ray CT to reconstruct the components within HT-PEMFC MEAs in 3D, enabling multi-physics and multiphase coupling simulations. Through controlled variable decoupling analyses of the changes in MEA morphology, insights into the impact of individual variables on MEA performance, along withthe relationships between different elements or variables, can be determined. This methodology therefore offers a deep learning approach to understanding the mechanisms of MEA performance, guiding the design of future high-performance MEAs.

2. Results and Discussion

PVP-PES membranes offer a combination of benefits and limitations in fuel cell applications. PVP acts as an efficient proton acceptor, enhancing fuel cell performance, while its blending with PES imparts thermal stability and mechanical integrity, effectively reducing the excessive swelling associated with pure PVP in aqueous environments. Nevertheless, this membrane system encounters significant drawbacks, including hydrogen crossover and PA leaching, which constrain its long-term viability in HT-PEMFC operations. To investigate the durability of this PVP-PES membrane-based MEA in HT-PEMFCs, accelerated stress tests (AST) were applied. ASTs can expedite processes such as PA leaching and catalyst degradation in HT-PEMFCs. Compared to durability testing under constant current density, ASTs can achieve an accelerated effect about five times faster.[43] The 72-hour AST of an MEA based on a PVP-PES membrane under repeated chronopotentiometry at 0.6 and 1 A cm^{-2} is shown in **Figure 1a**. During the AST, the cell was operated under open circuit voltage (OCV) conditions for 10 min every six hours. The OCV of the MEA was relatively low, with a maximum value of ≈0.75 V, gradually decreasing to ≈0.7 V during the AST. This is significantly lower than the typical OCV of ≈1 V for PEMFCs. This discrepancy may be related to the inherent hydrogen permeability of the PVP-PES membrane, although the possibility of membrane perforation occurring during the AST cannot be ruled out. The voltage variation at 0.6 A cm^{-2} and 1 A cm^{-2} showed that the voltage gradually increased on the first day, but a slow decline began on the second day. However, even after 72 h, the voltage remained significantly higher than the initial value. In Figure 1b, the polarisation curves at different stages correspond to the phases of the AST. Specifically, days 1, 2, 3, and 4 correspond to the initial measurement before AST, and the measurements taken after 24, 48, and 72 h of testing, respectively. The

A. Rack, B. Lukic
The European Synchrotron Radiation Facility
71 Avenue des Martyrs, Grenoble 38000, France
S. J. Haigh
Department of Materials
University of Manchester
Oxford Road, Manchester M13 9PL, UK

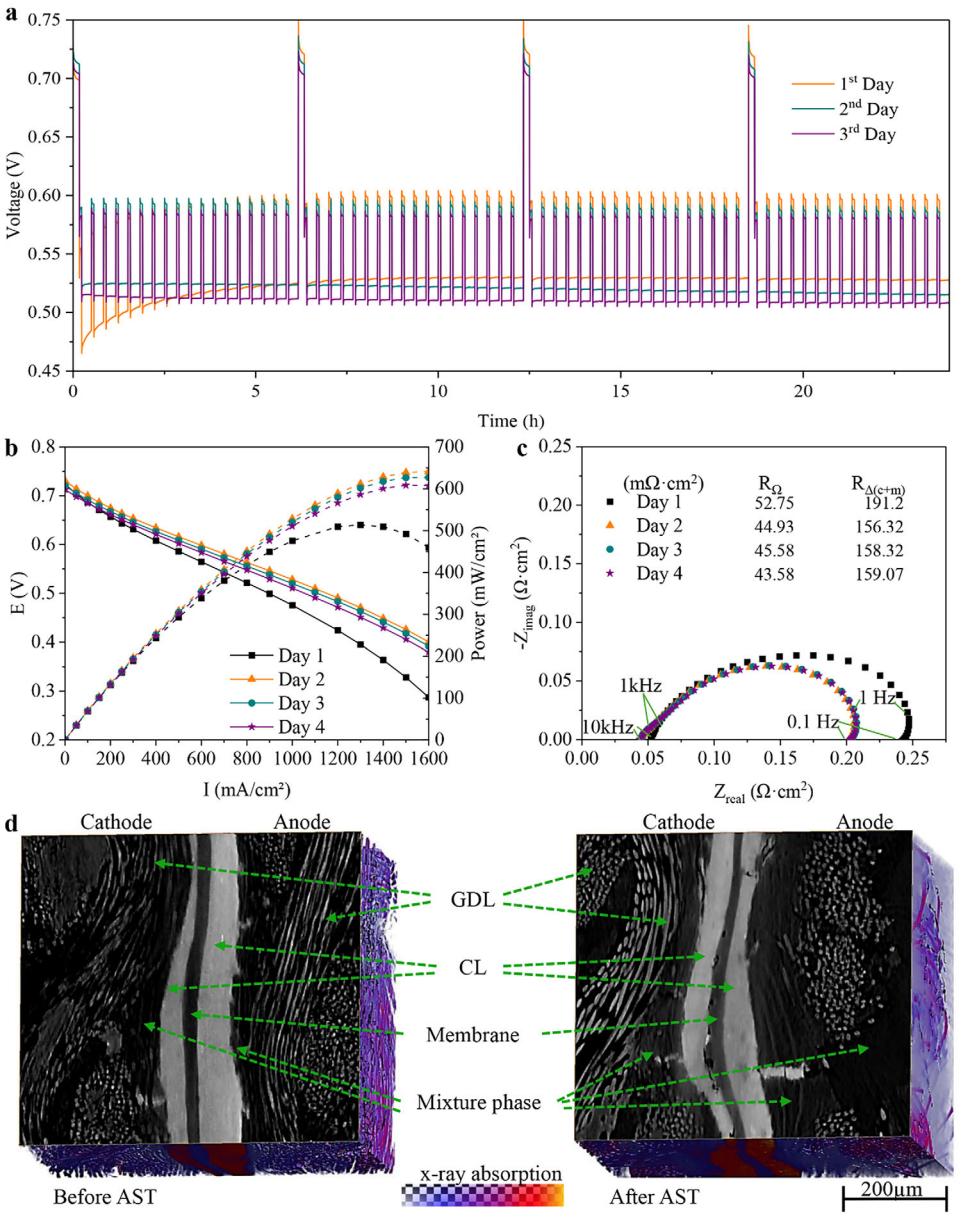

Figure 1. Electrochemical performance and durability of PVP-PES membrane-based HT-PEMFC 160 °C, anode: H_2 ($\lambda = 1.2$), cathode: Air ($\lambda = 2$) and X-ray CT images, a) AST, b) polarisation curves and c) EIS curves (Nyquist plots, DC: 0.5 A cm^{-2}, frequency:10 kHz–0.1 Hz), d) X-ray CT images before and after AST, the 2D grayscale slices and 3D volume rendering contain information about the X-ray absorption intensities of different materials.

polarization curves for day 1 and day 2 exhibit pronounced differences, particularly in the medium and high current density regions. Although the polarisation curves for days 2, 3, and 4 display slight variations, there is a clear trend of progressively decreasing peak power density over time. The EIS Nyquist curves corresponding to the polarisation curves are shown in Figure 1c. As the Nyquist curves obtained did not resolve the semi-circle at low frequencies, associated with mass transfer resistance, this component represents the combined charge transfer resistance and mass transfer resistance as $R_{\Delta(c+m)}$. R_Ω is used to denote the dominant ohmic resistance, primarily attributed to membrane resistance. The equivalent circuit for the Nyquist curves is shown in Figure S1 (Supporting Information). Similar to the polarisation curves, the Nyquist curve on day 2 exhibits significant differences compared to day 1. Importantly, after 24 h of AST, the resistance decreased, particularly in the $R_{\Delta(c+m)}$, whereas the Nyquist curves on days 2, 3, and 4 show no significant differences, only fluctuating slightly. Hence, while EIS is valuable for evaluating the overall electrochemical performance of HT-PEMFCs, its ability to provide detailed information on changes to specific materials within the MEA is limited. For instance, the miniature semicircles at high frequencies, which are often attributed to fast interfacial processes, remain poorly understood and the factors influincing them remain somewhat open to interpretation.

Therefore, while EIS can highlight trends and behaviours, it cannot conclusively define the contributions of individual materials within the MEA.

As observed from the AST and polarisation curves, the electrochemical performance exhibits a rapid increase during the initial stage on day 1, followed by stabilisation and a gradual decline after day 2. The initial rise in performance can be attributed to the activation process, wherein electrochemical reactions stabilise, catalyst utilisation improves, and PA redistributes within the membrane, thereby enhancing proton transport pathways.[44,45] During the early stage of operation, non-uniform PA distribution may lead to elevated ohmic resistance, which gradually decreases as PA migration facilitates more efficient ionic conduction. Additionally, EIS results indicate a reduction in charge transfer resistance after the first day, suggesting improved electrode kinetics and interface stability. Moreover, membrane thinning during initial operation may also contribute to a reduction in ohmic resistance, further enhancing proton conductivity.[22] Although HT-PEMFCs do not rely on water for proton conduction, residual water or solvent traces in the membrane may initially affect ion transport.[46] As these components equilibrate over time, they may further contribute to the observed improvement in performance before reaching a steady-state condition.

Representative 2D slices from 3D CT reconstructions of the MEA based on the PVP-PES membrane before and after AST, as shown in Figure 1d, provide more direct and insightful material information. The full 3D reconstruction approach will be discussed later in the manuscript but even these 2D slice X-ray CT images reveal that the MEA exhibits more morphological "defects" after AST, such as small pores on the cathode side of the membrane caused by water generated at the cathode, membrane bending due to thickness irregularities, catalyst migration, and catalyst cracks. These morphological "defects" could induce a series of alterations in physical fields, such as hydrogen crossover, gas permeability, triple-phase boundary dynamics, and charge transport. These factors collectively contribute, either directly or indirectly, to electrochemical performance and degradation. Therefore, a systematic study with controlled variables is warranted to elucidate their respective roles and contributions. The details of these morphological defects are shown in Figures S2–S4 (Supporting Information). The swift, significant and resolvable degradation of the PVP-PES membrane provides an excellent opportunity to study the impact of the phenomena observed through image-based modelling. By systematically extracting and addressing the various morphological defects, we can construct distinct models to facilitate a decoupled analysis of each defect's individual influence on PEMFC performance. This methodological approach enables a comprehensive assessment of how specific degradation phenomena, such as pore formation or catalyst migration, affect the overall electrochemical behaviour of the fuel cell. Ultimately, this will enhance our understanding of the underlying degradation mechanisms and inform strategies for material optimisation and durability improvement.

Before the post-AST behavior is analysed further, it should be noted that the initial OCV before AST is already lower than the expected ≈1 V for a well-functioning HT-PEMFC membrane, indicating the presence of hydrogen crossover.[22] This is further supported by the tilting of the Cyclic voltammetry (CV) curves, as shown in Figure S5 (Supporting Information). Despite this, micro-CT analysis of the fresh MEA did not reveal any micron-scale pinholes or significant structural defects that could directly account for the increased crossover. This suggests that hydrogen crossover may be attributed to sub-micron or nanometre-scale defects, which are beyond the detection limits of μ-CT. Furthermore, the PVP-PES membrane is a composite material, and phase separation between different polymer domains could further contribute to hydrogen permeability.[17]

Previous studies have demonstrated that a reduction in pore and fibre structure can infer PA migration, which in turn may drive migration within the microporous layer (MPL) and CL.[41] This inference is supported by the clear differences observed in Figure 1d, particularly in the grey region near the CL, which transitions from a structure characterised by fibres and pores to a more uniform grey area after AST. The mixture phase observed in Figure 1d consists primarily of leached PA, PTFE binder, carbon fibres, carbon black, and possibly water, originating from the MPL and GDL.[41] The presence of this phase suggests material redistribution within the MEA during operation, influencing proton conduction and mass transport. Due to the inherent resolution limitations of micro-CT, nano-micro scale structures with low atomic mass—such as fine pores in the MPL and localised PA accumulations—cannot be fully resolved, leading to segmentation into two primary phases: a pore phase and a mixture phase. This limitation means that while micro-CT effectively captures the macroscopic distribution of PA and structural changes, it may underestimate the extent of PA migration and interactions with carbonaceous materials. However, despite the inability to further segment the mixture phase into finer components, its morphological variations and changes in porosity distribution still provide indirect evidence of material migration.[47] Differences in mixture phase volume fractions among MEAs indicate variations in PA retention, PTFE redistribution, and carbon structural integrity, which could directly affect long-term electrochemical performance. To complement these findings, high-resolution techniques including FIB-SEM were employed to further analyse the composition and spatial distribution of the mixture phase.

Although HT-PEMFCs avoid issues related to water management, excessive leaching of PA from the membrane to the electrodes resembles water flooding observed in low-temperature PEMFCs.[3,48] Additionally, while the water produced at the cathode rapidly turns into steam at high temperatures, it also accelerates the leaching of PA.[45,49,50] Thus, managing PA in HT-PEMFCs shares similarities with water management in low-temperature PEMFCs. Knowing this, it can be understood that in HT-PEMFCs based on PA-doped proton exchange membranes, the membrane's ability to control PA leaching can significantly affect the formation of the triple-phase boundary in the CL and the mass transport within the GDL.[3,47]Yet, while morphological defects and PA leaching can be observed after AST in Figure 1d, the observed performance later in the AST still shows an improvement compared to the initial performance during the AST. Therefore, the observed morphological "defects" are not necessarily the cause of the eventual performance degradation, and instead could be the driver of the performance improvement. Unfortunately, these morphological "defects" might be interrelated and occur simultaneously, making it challenging to isolate and compare them through intervention-based experiments to investigate their impact on performance. Consequently, the

development of a new protocol to address this issue is necessary. A multiphase and multi-physics model, based on CT scan-derived models, needs to be established to enable the extraction and decoupled analysis of individual defects. This approach will facilitate the re-coupling of the effects of single or multiple defects on PEMFC performance.

Figure 2 presents a protocol for a multi-physics and multiphase visualization simulation, based on micron-scale X-ray CT and nanoscale FIB-SEM 3D scanning. As shown in Figure 2a-i, segmentation of the membrane, CL, and pores can be performed based on the grayscale values in the X-ray CT images. Using the island selection tool in Avizo (see methods), the mixture phase can be separated from the GDL, which is characterised by carbon fibre structures based on the different contrasts produced by the difference in density between these two materials.

This segmentation approach enables the capture of detailed information on membrane pores, CL cracks, CL migration, and PA leaching. As shown in Figure 2a-ii, slice-by-slice segmentation enables the construction of a 3D visual model framework. This, in turn, allows for micron-scale pore network analysis, as illustrated in Figure 2a-iii, providing information such as porosity and facilitating permeability simulations. For the nanopore structures within the CL and the mixture phase, including the MPL, the higher spatial resolution achievable with FIB-SEM imaging was exploited, as demonstrated in Figure 2a-iv,v. This approach facilitates the reconstruction of these nanostructures, enabling subsequent pore network analysis and permeability simulations. The reconstruction of these 3D models, along with segmentation, pore network modelling, and permeability simulations, are all conducted within Avizo (see methods). The permeability values of different MEA components have been extracted from absolute permeability simulations and are provided in Table S1 (Supporting Information). The GDL exhibits the highest permeability, measured at 8.53×10^{-12} m^2, due to its relatively large pore size and high porosity. In contrast, the mixture phase, which includes the MPL, has a significantly lower permeability of 1.36×10^{-12} m^2, reflecting the increased tortuosity and reduced pore connectivity within this region. Similarly, the CL has a permeability of 1.39×10^{-12} m^2, which is slightly higher than that of the MPL but still considerably lower than that of the GDL, consistent with its fine microstructure and high material density. These permeability values play a crucial role in the multiphase and multi-physics modelling used in this study. However, due to differences in the 3D reconstruction techniques and the spatial scales used for different MEA components, adjustments are necessary to accurately represent gas transport behaviour across the layers. These corrections and their impact on the simulation framework will be elaborated in later sections.

Based on the 3D structural scans, multiphase segmentation, and the acquisition of porosity and permeability parameters, a model as shown in Figure 2b-i was established. This model was then meshed for finite element simulations, enabling multi-physics visualization simulations that couple the fuel cell electrochemical module with the free and porous media flow module in COMSOL. The simulations yield the results shown in Figure 2b-i-i–v, including electrode potential with respect to ground, electrolyte potential, gas mole fraction with streamlines, and water mole fraction distribution respectively. In Figure 2b-ii,iii, the green and cyan arrows represent the electrode current density vector and the electrolyte current density vector, which correspond to proton and electron conduction. The multi-slice distribution of potential also reveals the voltage loss across the MEA. These results demonstrate that the multi-physics field distributions are morphology-based, and the previously mentioned morphological "defects" have caused differential distributions in these physical fields. While the impact of individual physical fields on MEA performance is significant, it is the synergistic interaction among multiple physical fields that ultimately determines the MEA's overall performance. By integrating the various physical fields shown in Figure 2b-ii–v, a four-phase distribution and interface, including electrolyte, catalyst, gas, and water, can be obtained, as illustrated in Figure 2b-vi.

To better demonstrate the advantages of the CT-based model over simplified 3D models and to analyse the impact of certain morphological defects, additional model details are presented in **Figure 3**. The potential and current vector distributions of the electrolyte and electrode are shown in Figure 3a,b, where it can be seen that the CT-based model and simulation align well with the morphology of the membrane and catalyst, allowing for a more accurate investigation of interfacial changes compared to simplified models. Additionally, the irregularity of the membrane can be seen to increase the interfacial area to some extent. The current distribution in the electrode also varies with the structure of the carbon fibres, as well as the morphology and cracks in the catalyst. The hydrogen flux streamlines are shown in Figure 3c and reveal that cracks in the catalyst can disrupt hydrogen flow. Similarly, Figure 3d demonstrates that the morphological structure of the MEA affects hydrogen flow rates. As previously mentioned, on the cathode side of the PVP-PES membrane, dissolution due to water production could result in pore formation. Figure 3e,f, which depict oxygen flux streamlines and water distribution, provide unexpected insights: these so-called pores are not filled with gas but exhibit a high water content. In HT-PEMFCs, this stored water could potentially lead to PA leaching, forming diluted PA, which can still function as an electrolyte for proton conduction. Moreover, these pores can play a role in regulating the humidity within the MEA.

Building on the aforementioned multiphase, multi-physics integrated visualization model, it is possible to further explore the impact of individual elements or variables on charge distribution, gas transport, and water distribution by decoupling these factors. This can be achieved by modifying the morphological "defects" during segmentation, allowing for the extraction and adjustment of single elements or variables. Through this approach, the influence of each isolated factor on the physical fields and overall performance can be systematically investigated. Since CT is a tomographic imaging technique, adjustments to the segmentation of each individual 2D slice can be used to modify the overall 3D structure. This allows for the step-by-step alteration or elimination of each specific morphological "defect". As illustrated in **Figure 4**, decoupling can be achieved by reassigning regions such as membrane pores, catalyst cracks, and catalyst migration. This process allows for the establishment of relared, but specifically modified, models: ① the original model, "② no membrane pores," "③ no catalyst cracks," and "④ no catalyst migration". Additionally, models named "⑤ flat membrane" and "⑥ mixture phase sShrink" have been established. The process of creating these isolated defect models, along with the structural changes and

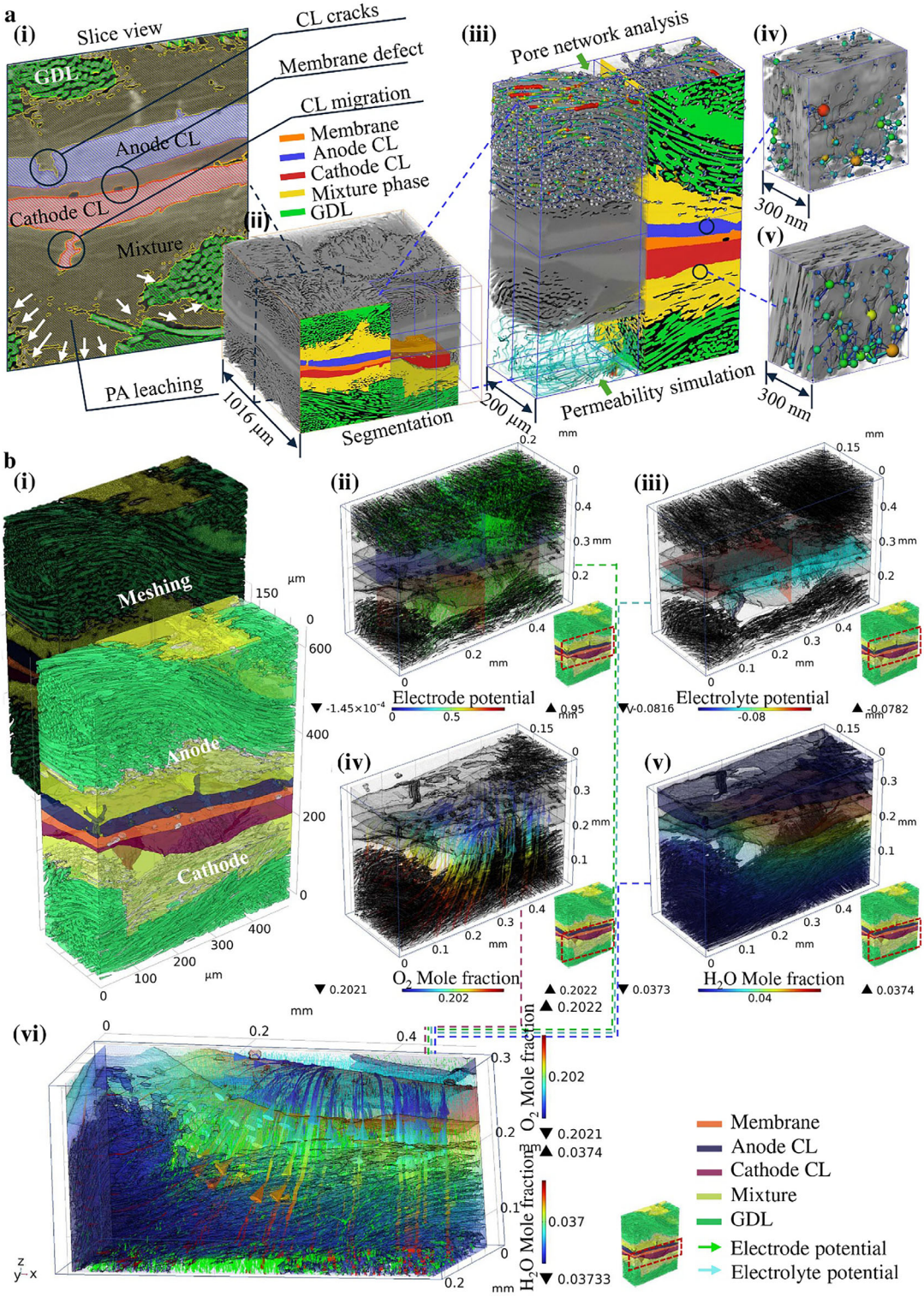

Figure 2. The protocol for 3D modelling and multiphysics coupled visualization s"imulation. a) CT-based segmentation, pore network and permeability analysis. i) Slice view of component segmentation, ii) volume rending and 3D segmentation, iii) pore network and permeability simulation of GDL, iv) FIB-SEM based pore network and permeability simulation of CL and v) FIB-SEM based pore network and permeability simulation of MPL. b) Electrochemistry-based multi-physics visualisation simulation. i) 3D model of PVP-PES membrane-based MEA and meshing, ii) Electrode potential with respect to ground (arrow volume: electrode current density vector), iii) Electrolyte potential (arrow volume: electrolyte current density vector), iv) Total flux streamline of O_2, v) Water mole fraction distribution surface, vi) Multiphysics and multiphase interface.

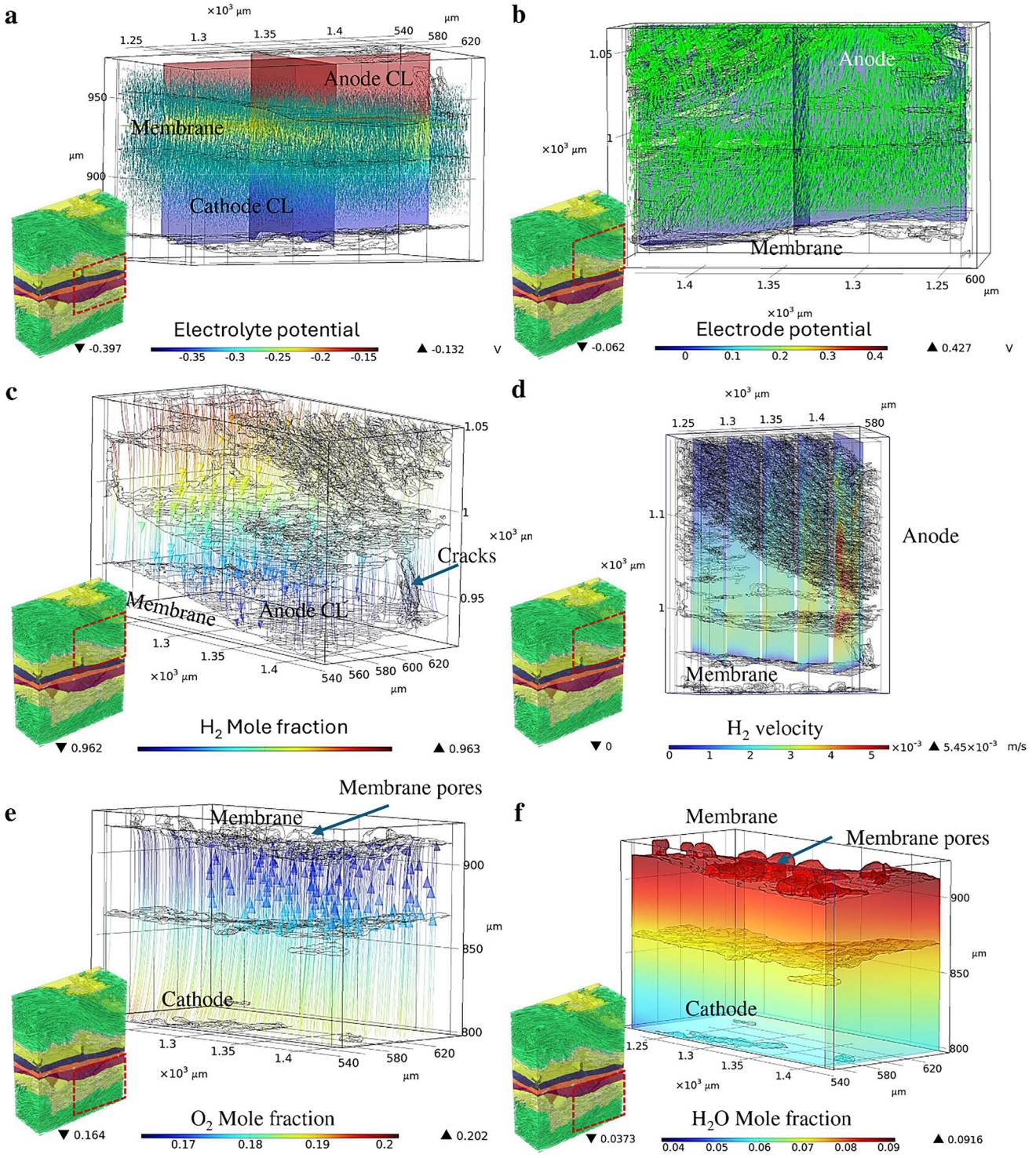

Figure 3. Multiphase and multiphysics coupling with the morphological conformity of the CT-based MEA with PVP-PES membrane model. a) Electrolyte potential (arrow volume: electrolyte current density vector), b) Electrode potential with respect to ground (arrow volume: electrode current density vector), c) Total flux streamline of H_2, d) H_2 velocity distribution, e) Total flux streamline of O_2, f Water mole fraction distribution surface.

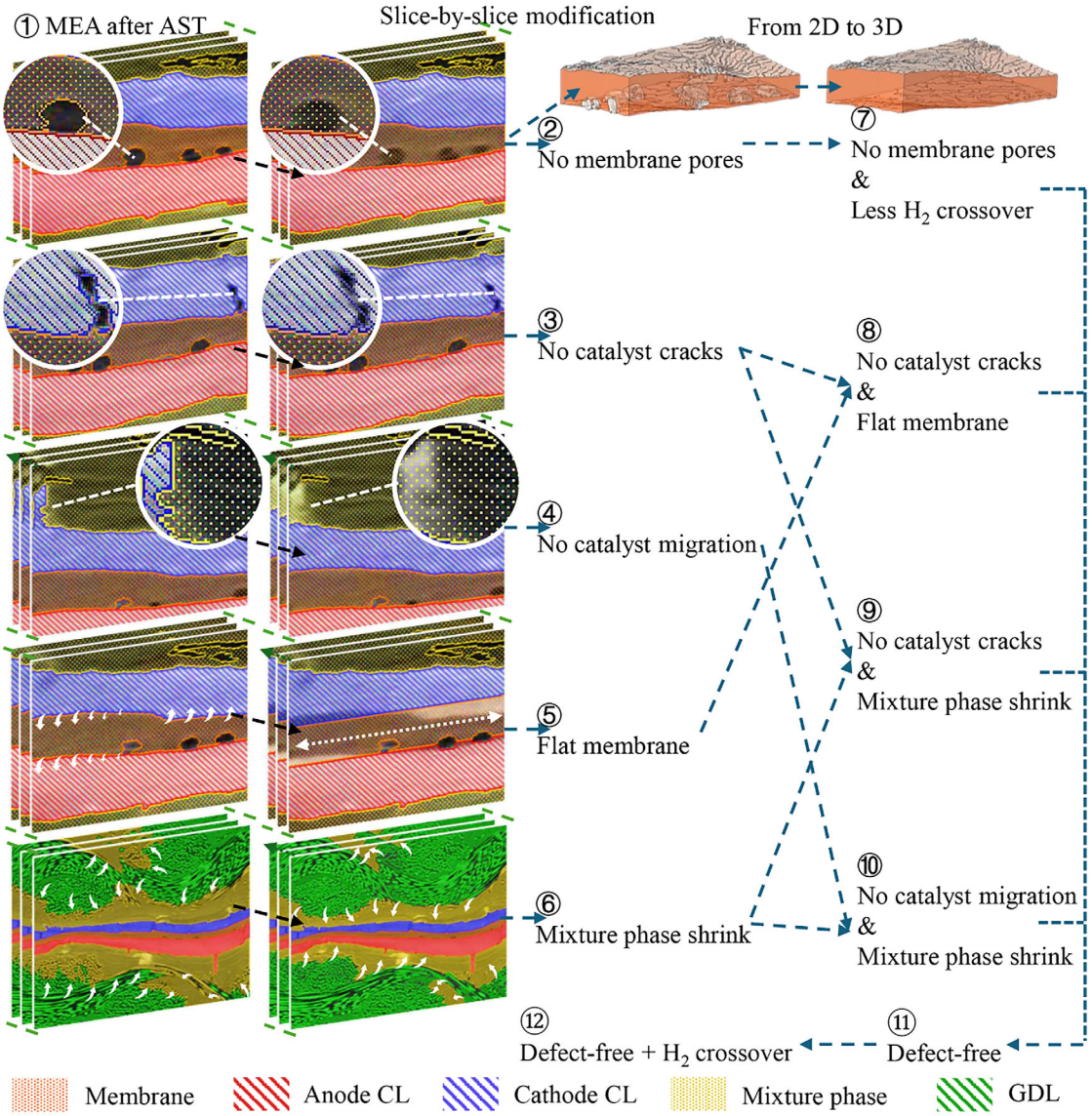

Figure 4. The protocol for decoupled and recoupled models with controlled variables through image segmentation.

condition alterations, is detailed in **Table 1**. These models were refined by modifying the 3D structure through slice-by-slice adjustments of cross-sectional images. More detailed information is provided in Figures S6–S10 (Supporting Information). Models were also produced which combine defects. These will be described later but are also listed in Table 1 for completeness.

The electrochemistry-based simulations enable the characterization of potential and current distributions within the MEA at various output voltages, as depicted in **Figure 5a** and Video S1 (Supporting Information). This approach facilitates the derivation of polarization curves and power density curves. Simulated polarisation curves for the MEA based on the PVP-PES membrane after AST, as well as for the decoupled models with individual morphological "defects," are presented in Figure 5b. Importantly, while the simulated polarization and power density curves do not perfectly match the experimental data, they exhibit similar characteristics, both showing a decrease in OCV due to hydrogen crossover. The comparison between the simulated and experimental polarization curves (Figure S11, Supporting Information) indicates a strong correlation, reflecting the model's capability in approximating the multiphase and multi-physics behaviour of the MEA after AST. While the model effectively captures key trends, minor deviations remain due factors such as the computational domain size. In spite of this, this result suggests that the structural and transport properties extracted from the CT-based model provide a representative basis for electrochemical performance predictions. Additionally, while the model does not explicitly include impedance contributions from flow-field plates, wires, and other external components, their impact on overall performance appears to be minimal within the simulated domain.

Before outputs from the simulations are considered further, it is appropriate to acknowledge that the modelling approach used involves various assumptions and limitations. The

Table 1. Modification, structure and condition changes of decoupled and recoupled models with controlled variables through Image Segmentation.

	Modification	Change of structure and condition
①MEA after AST	Original model reconstructed from the 3D scan of PVP-PES membrane-based MEA after AST without modification	
②No membrane pores	The pore structures on the membrane are reassigned slice-by-slice back to the membrane through segmentation adjustments.	The 3D pore structures on the membrane have been eliminated.
③No catalyst cracks	The cracks in the CL are reassigned slice-by-slice back to the CL through segmentation adjustments.	The 3D crack structures in the CL have been eliminated.
④No catalyst migration	The catalyst migrating to the MPL and GDL is reassigned to the mixture phase slice-by-slice.	The migration of the catalyst into the electrode has been eliminated.
⑤Flat membrane	By smoothing the membrane based on its average thickness, while retaining the membrane pores and catalyst morphology	A model with a flat membrane can be obtained
⑥Mixture phase shrink	By applying volumetric shrinkage to the segmented mixture phase in Avizo, the regions with carbon fibre structure in the shrunk mixture phase are then reassigned to the GDL.	The migration of PA components caused by PA leaching, along with the associated movement of mixed components such as the MPL, has been reduced, leading to improved mass transport of hydrogen and oxygen.
⑦No membrane pores and Less H_2 crossover	Based on Model ②, the hydrogen crossover was adjusted to reach the levels observed before the AST.	Hydrogen crossover caused by perforations in the membrane was taken into consideration.
⑧No catalyst cracks and Flat membrane	Combine ③ and ⑤	
⑨No catalyst cracks and the Mixture phase shrink	Combine ③ and ⑥	
⑩No catalyst migration and Mixture phase shrink	Combine ④ and ⑥	
⑪Defect-free	Combine ① – ⑩	
⑫Defect-free + H_2 crossover	Based on model ⑪ but increase the H_2 crossover to match that of model ①	

computational domain does not explicitly include the flow-field channels and ribs, meaning that potential compression effects on the GDL and variations in reactant distribution due to channel-rib interactions are not accounted for. Additionally, while the membrane morphology was modified in the model, the internal pore structure of the CL was assumed to remain unchanged, which may not fully capture the local variations induced by membrane deformation. Furthermore, resistance validation was not included, as real-time high-frequency resistance data was not available in this study. Finally, the domain size is limited by computational constraints, preventing the simulation from fully representing larger-scale structural variations within the MEA. Certain details that cannot be reconstructed in 3D are treated as homogeneous and are instead accounted for through parameterized modelling. These factors should therefore be considered when interpreting the results, as they may represent potential sources of error.

As expected, not all defects result in performance degradation. A preliminary analysis reveals that the performance of the MEA with "②no membrane pores" remains largely unchanged compared to the original MEA. This suggests that the disadvantage of reduced contact between the membrane and catalyst caused by membrane pores may be partially offset by the advantage of humidity regulation provided by the pores, as mentioned earlier. In contrast, the models with "③no catalyst cracks" and "⑥mixture phase shrink" show performance improvements. The detrimental effects of catalyst cracks and PA migration are evident, but this is specific to the current conditions. Conversely, the "⑤flat membrane" and "④no catalyst migration" models exhibit decreased performance. This involves more complex interfacial issues and also indicates that the model is responsive to these morphological defects.

In the following sections, we provide a more detailed case study, combining the visualisation of the multiphase and multiphysics models for an in-depth analysis of these elements. Furthermore, we investigate the effects of selectively re-coupling the decoupled elements, which may shift the relative advantages and disadvantages of the morphological defects. For example, for specific single-variable conditions, the presence of membrane pores are shown to have minimal impact on performance when hydrogen crossover effects are not considered. Furthermore, membrane bending and CL migration contribute positively to performance, whereas PA migration and catalyst cracks have a detrimental effect and localized thinning of the membrane is a significant cause of hydrogen crossover. In the case where membrane pores are absent, hydrogen crossover is substantially reduced, thereby improving performance, as shown in Figure S12a (Supporting Information).

After decoupling the different elements or variables, they can be systematically re-coupled in a well-founded manner to explore their synergistic effects. A reduction in membrane pores can decrease hydrogen crossover. Membrane bending may lead to the deformation of the CL, while an MEA with a flat membrane may exhibit fewer catalyst cracks. Additionally, PA migration can induce the migration of other components, linking CL cracks with CL migration. Various combinations of these factors are possible,

but this study specifically explores the combinations illustrated in Figure 4, which are listed as models ⑦–⑩ in Table 1.

By pairing these decoupled individual elements these models are able to directly analyse the overall impact of the two MEA structures. The coupling of "③ no catalyst cracks" and "⑤ flat membrane" is illustrated in Figure 5c. Although removing catalyst cracks improves performance based on the original MEA, eliminating catalyst cracks in the MEA with a flat membrane leads to a decrease in performance. Thus, the impact of catalyst cracks on MEA performance is influenced by the membrane's flatness, which extends to considerations of the membrane's mechanical properties. Furthermore, the results of model ⑩ coupling "③ no catalyst cracks" and "⑥ mixture phase shrink" are also noteworthy. As shown in Figure 5d, the elimination of catalyst cracks on the basis of "mixture phase shrink" not only failed to improve performance but led to a decrease in performance. It is therefore evident that these catalyst cracks can play different roles under varying mass transfer conditions. The "⑥mixture phase shrink" model represents, to some extent, improved mass transport. Together these data demonstrate that catalyst layer cracks have varying effects depending on the mass transport conditions. Similarly, although catalyst migration can enhance performance under specific conditions, its benefits become less pronounced under the conditions of "⑥ mixture phase shrink," as illustrated in Figure 5e. In summary, these morphological "defects" can have both beneficial and detrimental effects on MEA performance, and their interactions can be mutually constraining. This interplay may explain the observed fluctuations in MEA performance during the AST process, potentially reflecting the changing balance or advantages and disadvantages among these morphological "defects". It is precisely because the so-called morphological "defects" interact and balance each other that their impact on performance can be controllable. For instance, high-performance catalysts prone to cracking could be paired with membranes that possess high mechanical strength and are less prone to bending or deformation, thereby potentially turning these cracks into factors that enhance performance. This approach offers a novel perspective for the design and manufacturing of MEAs, suggesting that leveraging these defects could strategically improve performance. The model and polarisation curve in Figure 5 serve as representative comparisons. The radar chart in Figure S13 (Supporting Information), illustrating the power density of different models at 0.4 V, provides a more intuitive comparison of the variations.

The establishment of the above protocol not only allows the extraction of polarisation curves to compare the performance impacts caused by single-element decoupling and multi-element recoupling but also enables a multi-perspective analysis of the mechanisms through the distribution of multiphase and multi-physics fields. **Figure 6** illustrates an example of the comparative analysis of single-element decoupling and dual-element coupling in multiphase and multi-physics systems under flat membrane and no-catalyst-cracks conditions. This analysis corresponds to the polarization curves shown in Figure 5c. The comparison of the vector current distribution in the electrolyte and electrode between Figure 6a-i,b-i provides a clear explanation for the performance degradation observed after flattening the membrane. Although the MEA based on the flat membrane exhibits a uniform current distribution, the original MEA, with its tortuous interface, allows multi-angle and multi-path current transfer between the electrode and the membrane, significantly increasing the interfacial area. However, when calculating the current density, the effective area of the MEA is usually considered, which greatly enhances the utilization of the MEA with the same size. The comparison of Figure 6a-i,c-i shows that the removal of catalyst cracks can increase the current vector density in this region, thereby enhancing performance.

However, the effects of the changes discussed above extend beyond what can be explained by the variation in current density vectors alone, as the differences between Figure 6b-i,c-i are not easily elucidated by this single physical field. When coupling the "⑤ flat membrane" element with the "③ no catalyst cracks" condition in model ⑧, the current vector density in the crack regions did not increase; instead, it showed an overall decrease. Figure 6b–d-iii shows the streamlines of H_2, where the arrow vectors are distributed with equal arc length. In Figure 6b,c-iii, near the cracks and membrane surface, the arrows vary in colour, size, or direction, representing gas disturbances. These disturbances indicate that the gas tends to flow turbulently near uneven surfaces or catalyst cracks. In contrast, the arrow vectors in Figure 6d-iii are uniform in direction, colour, and size, suggesting that the gas flow is more laminar. Turbulent H_2 flow can more effectively promote reactions within the catalyst compared to laminar flow, as indicated by the hydrogen mole fraction distribution. By employing the proposed protocol for single-element decoupling, the influence of the GDL on gas transport remains consistent across the different models shown in Figure 6. However, under the "⑤ flat membrane" and "③ no catalyst cracks" conditions, the hydrogen mole fraction at corresponding positions is relatively higher. Although this difference is not substantial in magnitude, given the use of humidified pure hydrogen, even minor variations in mole fraction reflect significant changes in the amount of hydrogen. When the hydrogen transport conditions within the GDL are the same, a higher hydrogen mole fraction at the catalyst–membrane interface indicates reduced consumption by the reaction. The H_2 flow velocities shown in Figure 6a–d-iv further highlight these differences. Variations in flow velocity near catalyst cracks induce disturbances in the flow. In the absence of catalyst cracks, uneven membrane surfaces can still enhance overall flow velocity, leading to disturbances. However, when both catalyst cracks are eliminated and the membrane is smooth, the hydrogen flow velocity remains uniform. Figure 6a,b-v further illustrate these structural differences across different models, providing a clearer depiction of the impact of each configuration.

In addition to the decoupling and recoupling mechanism analysis of the elements "③ no cracks" and "⑤ flat membrane," the approach developed in this work provides a multi-perspective explanation of the effects of other decoupling and recoupling factors. The fitting structures of different models are illustrated in Figures S14–S58 (Supporting Information), highlighting the variations in the distribution of different physical fields.

The discussion of Figure 5 highlights the complex role that "defects" play in MEA performance. As noted, certain defects can be either beneficial or detrimental, depending on their interactions with other factors. This observation suggests that strategic manipulation of defects could potentially enhance performance. To further explore this concept, it would be valuable to compare

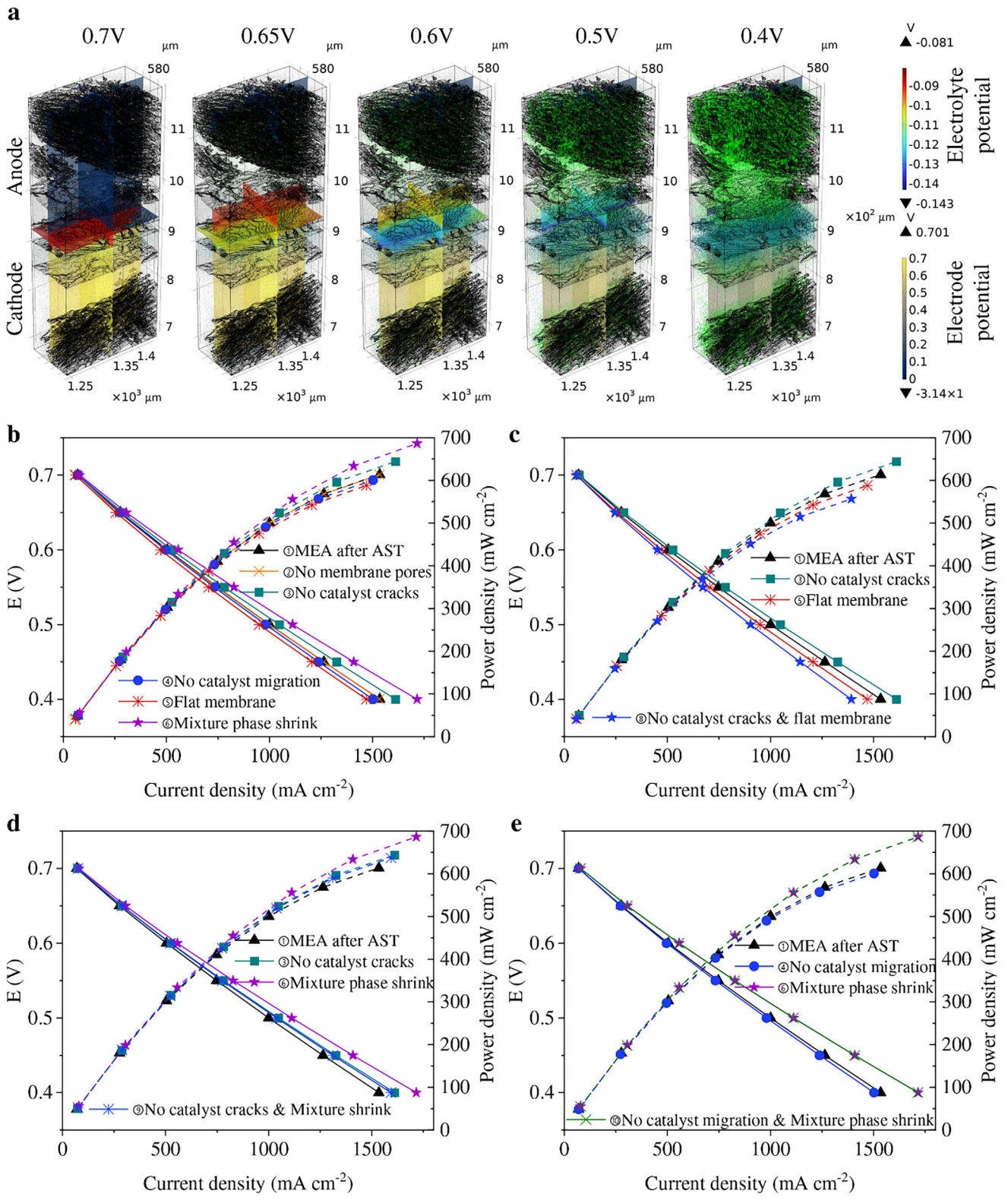

Figure 5. Polarization and power density curves from controlled variable decoupled and coupled simulations of PVP-PES membrane-based MEA after AST. a) current and potential distribution at different cell voltage (arrow volume: electrode (green) and electrolyte (cyan) current density vector), b) single-variable decoupling, c–e) Two-variable coupling.

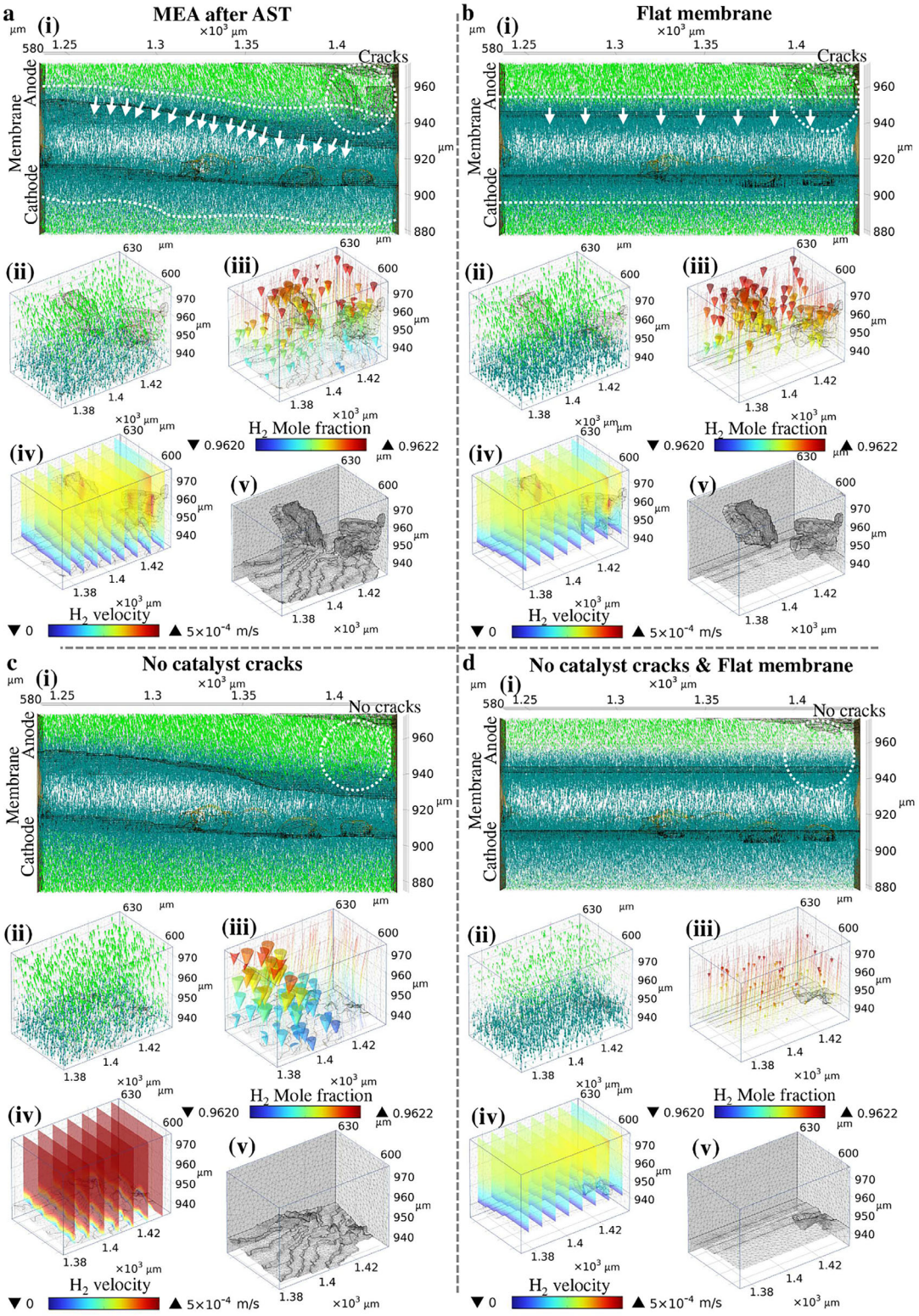

Figure 6. Comparative analysis of single-element decoupling and dual-element coupling in multiphase and Multiphysics systems for flat membranes and no-catalyst-cracks conditions. a) PVP-PES membrane-based MEA after AST, i) side view of current distribution between membrane and CL (arrow volume: electrode (green) and electrolyte (cyan) current density vector) at 0.4 V, ii) 3D view of current distribution between membrane and CL of cracks area at 0.4 V, iii) Total flux streamline of H_2 with mole fraction distribution at 0.7 V, iv) H_2 velocity distribution at 0.7 V, v) 3D mesh structure of cracks area. b) ③ Flat membrane module, c) ⑤ No catalyst cracks module and d) ⑧ No catalyst and Flat membrane module.

the performance of a completely "defect-free" MEA against MEA after AST. A "⑪ defect-free model" was introduced, as depicted in Figure 4. To isolate the effects of hydrogen crossover, an additional model was developed: a defect-free structure with hydrogen crossover levels matching those of "model ①" after AST, referred to as "⑫ defect-free + H_2 crossover". Detailed descriptions of these two models are provided in Table 1, and the corresponding polarization and power density curves are presented in Figure S12b (Supporting Information). As illustrated in Figure S12b (Supporting Information), the performance of the ⑪ defect-free model is slightly superior to that of the ① MEA after AST. However, when accounting for the impact of hydrogen crossover, the performance of ⑫ Defect-free + H_2 crossover closely aligns with that of the model ① MEA after AST. This observation does not imply that the so-called defects have no significant effect on performance, nor does it necessarily indicate the beneficial or detrimental nature of these defects. Instead, it underscores the complex synergistic interactions among these defects.

3. Conclusion

Through the development of a multi-phase and multi-physics image-based 3D model, derived from data from the advanced structural characterization of real MEAs, the impact and interplay of materials changes can be predicted. The decoupling of individual elements, such as catalyst cracks, membrane pores, and phase migration, allowed for a detailed examination of their isolated impacts on MEA performance, demonstrating that morphological features traditionally viewed as defects can, under certain conditions, enhance gas transport and catalytic activity by promoting local turbulence and increasing interfacial area, which is beneficial for electrochemical reactions. In contrast, smooth membranes and crack-free catalysts, despite exhibiting uniform current and flow distributions akin to laminar flow, do not always translate to performance gains due to the reduced turbulence and mass transport benefits. This coupling analysis further revealed that the interplay between different elements can significantly alter overall performance, emphasizing that mechanical properties and electrochemical behaviors are deeply interconnected.

Overall, these findings underscore the importance of a holistic approach in MEA design, where cross-component interactions should be strategically leveraged. By understanding the complex synergies between morphological elements this work therefore offers a pathway for optimizing PEMFCs beyond conventional material improvements, contributing to the development of next-generation fuel cells with enhanced performance, efficiency, and durability.

4. Experimental Section

The Preparation and Test of PVP-PES Membrane-Based MEA: A PVP-PES solution was prepared by separately dissolving PES (Ultrason E7020P, BASF Co., Germany) and PVP (1300 kDa) in *N*, *N*-dimethylacetamide (DMAc), followed by blending at a mass ratio of 3:2 (PVP: PES). The final concentration of the PVP-PES/DMAc solution was adjusted to 1 wt.%. This polymer solution was deposited onto a polytetrafluoroethylene (PTFE) Petri dish using an ultrasonic spray-coating technique, with the substrate maintained at 150 °C on a hot plate to facilitate solvent evaporation. Following the deposition, the coated PTFE dish was subjected to thermal treatment in an oven at 80 °C overnight, ensuring initial solvent removal. The membrane was then further dried under vacuum at 130 °C for 3 h to eliminate any residual solvent, yielding a free-standing membrane with a thickness of 40 ± 3 µm. Subsequently, the membrane was immersed in a saturated PA solution and allowed to soak overnight to achieve effective PA doping.

The PA-doped PVP-PES membrane was placed between Celtec anode and cathode Pt-based electrodes with a Pt loading of 1 mg cm^{-2}. The GDL was made of woven carbon fiber cloth. Teflon gaskets with a thickness of 190 µm were stacked on both sides to ensure sealing. The assembled MEA was then hot-pressed at 140 °C under a pressure of 100 psi for four minutes. After hot pressing, the MEA was mounted in a Scribner fuel cell fixture with an active area of 5 cm^2 and connected to an 850 Fuel Cell Test System for performance testing.

The MEAs were tested under conditions where compressed air and hydrogen were introduced to the cathode and anode, respectively, with stoichiometric ratios of 2 for air and 1.2 for hydrogen, at a temperature of 160 °C. Polarisation curves were obtained by progressively discharging from the OCV to 0.1 V in increments of 0.1 A, with each increment held for 5 s. In the EIS measurements, a Gamry Reference 3000 workstation was used with a perturbation magnitude of 10 mV (RMS). Galvanostatic EIS was performed at a current density of 0.5 A cm^{-2}, covering a frequency range from 10 kHz to 0.1 Hz with 10 points per decade to produce Nyquist plots. The MEAs underwent an AST protocol involving repeated chronopotentiometry, with operation at 0.6 A cm^{-2} for 4 min followed by operation at 1 A cm^{-2} for 16 min. The cells were maintained at OCV for 10 min between each cycle, and this pattern was repeated continuously for 6 h. CV measurements were conducted with the anode and cathode supplied with hydrogen and oxygen at flow rates of 33.4 and 140 ml min^{-1}, respectively. During these measurements, the working electrode's potential was cycled between 0.05 and 1 V at a scan rate of 100 mV s^{-1}.

X-Ray CT, FIB-SEM Scan and Data Analysis: Fresh MEAs and those subjected to AST were milled into 2 mm diameter discs using a laser cutting machine for scanning with the µ-CT at the ID19 beamline of the European synchrotron radiation facility (ESRF) in France and Carl Zeiss Xradia 620 Versa CT (Oxford Lasers, A Series/Compact System). For CT measurement in ESRF, A 250 µm thick single-crystal scintillator, cerium-doped (LuAG, Czech Republic), was paired with a pco. edge 5.5 s CMOS camera (PCO AG, Germany) and a U13 single-harmonic undulator to generate a peak photon energy of 80 keV. A 5× lens provided an isotropic voxel size of 0.65 µm, with a field of view of 2160 × 2560 pixels, allowing the entire sample to be captured in a single scan. The sample-to-detector distance was set to 200 mm to induce a propagation-based phase contrast effect. A total of 4000 projections were recorded at an exposure time of 300 ms per projection during a continuous 360° rotation. The data were reconstructed using standard filtered back projection with the ESRF's in-house NABU reconstruction package. For versa CT scanning, a 4× objective lens was used to accommodate a 2 mm sample field of view while maintaining a resolution of 1 µm. The scans were performed with a polychromatic source operating at a tube voltage of 60 kV, with an exposure time of 8 s and a rotation angle of 360°. FIB-SEM tomography was performed using a Zeiss Auriga 60 dual-beam system, generating a total of 676 FIB tomography slices. The tomography process was carried out at an accelerating voltage of 30 kV and a beam current of 20 pA, with each slice having a thickness of 9 nm. SEM images were captured at 5 kV with a pixel size of 3 nm, using both the in-lens (IL) and secondary electron (SE2) detectors. To protect the sample surface, a platinum layer was deposited over the sampling volume, followed by the engraving of lines to facilitate slice thickness verification. Component segmentation was performed in Avizo. A non-local means filter was utilized to improve image sharpness. Initially, machine learning techniques were employed to extract the membrane based on its shape characteristics. Subsequently, grayscale thresholding was used to isolate the catalyst and pore structures. Finally, island segmentation by slicing was used to separate the GDL from the mixture phase. Decoupled and coupled models were obtained by redistributing the morphological "defect" regions, thereby creating models where defects were removed from each element sequentially.

Multiphase and Multiphysics Visualization Simulation: The pore networks and permeability of the GDL, MPL, and CL were initially presimulated in Avizo. The pore structures were first extracted using interactive thresholding, followed by the removal of isolated pores through axis connectivity analysis. Subsequently, a pore network model and detailed pore and throat information were generated using the "separate objects" function. Permeability data were then obtained through an absolute permeability experiment simulation. The MEA model obtained from CT scanning was meshed in Avizo. CL, which involved more complex three-phase interfaces, was meshed with the finest refinement. Meshes from the different models were then imported into COMSOL for Multiphysics simulation. The pore-wall friction forces were modelled using wall diffusivity, which defaulted to Knudsen diffusivity. Knudsen diffusivity was determined from kinetic gas theory, connecting the mean free path of gas molecules with the pore diameter. The gas diffusivity specified in the Gas Phase node was adjusted by a correction factor to reflect that the gas pore volume fraction was less than 1. This adjustment could be implemented using the Bruggeman correlation, Tortuosity, or a user-defined method. For Tortuosity, options included setting an isotropic scalar value and defining anisotropic tensor values through Diagonal and Symmetric settings.

The fuel cell model incorporated mass transport, momentum transfer, and electrochemical processes to investigate the behavior of reactants and products across various components, including GDLs, gas diffusion electrodes, and the membrane. This model captured multiple physical phenomena through the application of specialized interfaces and equations. The key equations are shown below. Implemented within COMSOL Multiphysics, the model utilized Free and Porous Media Flow interfaces combined with Reacting Flow Multiphysics nodes to simulate complex transport dynamics within the fuel cell. It solved for key variables such as electrical and ionic potentials, species mass fractions, velocity fields, and pressure distributions, enabling a detailed analysis of the fuel cell's performance under varying operational conditions. Some parameters were obtained through simulation calculations, while the initial input parameters are listed in Table S1 (Supporting Information). Certain parameters in Table S1 (Supporting Information) were derived from electrochemical tests and simulations of scanned 3D models. Additionally, certain unknown and standard parameters were adopted from those utilized in simplified models found in the literature.[26,51]

Key Equations and Methods—Maxwell–Stefan Equations for Mass Transport: These equations are used to model the fluxes of species' mass fractions in the cell.

$$\nabla \times \left(-\rho\omega_i \sum_j \left(D_{ij}\nabla x_j + \left(x_j - \omega_j \right) \frac{\nabla p}{p} \right) + \rho\omega_i u \right) = 0 \tag{1}$$

where,

D_{ij}: binary diffusivity ($m^2\ s^{-1}$) ρ: fluid density ($kg\ m^{-3}$) ω: mass fraction u: velocity ($m\ s^{-1}$)p: pressure (Pa)D_{ij} can be calculated using the empirical equation derived from kinetic gas theory:

$$D_{ij} = \frac{10^{-3} \times T^{1.75}}{p\left[\left(\sum_k V_{ki} \right)^{\frac{1}{3}} + \left(\sum_k V_{kj} \right)^{\frac{1}{3}} \right]^2} \left(\frac{1}{M_i} + \frac{1}{M_j} \right)^{\frac{1}{2}} \tag{2}$$

where,

$\sum_k V_k$: molar diffusion volume

Key Equations and Methods—Navier–Stokes Equation for Momentum Transfer: This equation describes the momentum transfer in fluid flow.

$$\rho\left(u \times \nabla\right) u + \nabla p - \nabla \times \eta\ \left(\nabla u + (\nabla u)^T \right) = 0 \tag{3}$$

where,

η: fluid viscosity ($kg\ m^{-1}\ s$)

Key Equations and Methods—Darcy's Law (Coupled with Navier–Stokes for Porous Media): To study velocity distribution in porous media, Darcy's Law is incorporated into the Navier–Stokes equation.

$$\rho\left(u \times \nabla\right) u + \nabla p - \nabla \times \eta\ \left(\nabla u + (\nabla u)^T \right) = -\frac{\eta}{\kappa_p} u \tag{4}$$

where,

κ_p: permeability (m^2)

Key Equations and Methods—Brinkman Equations (Momentum Transfer in Porous Media): The flow within porous media is governed by the Brinkman equations, a combination of continuity and momentum equations:

$$\frac{\partial}{\partial t}\left(\varepsilon_p \rho\right) + \nabla \times\ (\rho u) = Q_m \tag{5}$$

$$\begin{aligned} &\frac{\rho}{\varepsilon_p}\left(\frac{\partial u}{\partial t} + \left(u \times \nabla\right) \frac{u}{\varepsilon_p} \right) = -\nabla p + \nabla \\ &\times \left[\frac{1}{\varepsilon_p} \left\{ \mu\left(\nabla u + (\nabla u)^T \right) - \frac{2}{3}\mu\left(\nabla \times u\right) I \right\} \right] \\ &- \left({k_p}^{-1}\mu + \frac{Q_m}{\varepsilon_p^2} \right) u + Force \end{aligned} \tag{6}$$

where,

Q_m: mass source or sink ($kg\ (m^2\ \times\ s^2)^{-1}$)

ϵ_p: porosity

μ: dynamic viscosity of the fluid ($kg\ m^{-1}\ s$)

Key Equations and Methods—Butler–Volmer Equation and Tafel Law (Electrochemical Reactions): The electrochemical reactions were modelled using both the Butler–Volmer equation and the Tafel equation. The Butler–Volmer equation provided a comprehensive description of the relationship between electrode potential and current density, accounting for both anodic and cathodic reactions. At higher overpotentials, this equation simplified to the Tafel equation, offering a linear approximation useful for analyzing reaction kinetics in these regions.

The Butler–Volmer equation is expressed as:

$$j = j_0\ [\exp\left(\frac{a_a z F \eta}{RT} \right) - \exp\left(-\frac{a_c z F \eta}{RT} \right) \tag{7}$$

where,

j: electrode current density (A m^{-2})

j_0: exchange current density (A m^{-2})

a_a and a_c: anodic and cathodic charge transfer coefficients

z: number of electrons transferred

F: Faraday constant (C mol^{-1})

η: overpotential (V)

R: universal gas constant (J $(mol \times K)^{-1}$)

T: temperature (K)

In regions of high overpotential, the Butler–Volmer equation reduces to the Tafel equation:

$$\eta = a + b\ \log\left(i\right) \tag{8}$$

where,

a: Tafel constant

b: Tafel slope

i:current density (A m^{-2})

To account for concentration dependence, the local concentrations of reactants and products were incorporated into the exchange current density j_0. This approach ensured that the reaction kinetics reflected the variations in species concentrations at the electrode interface, providing a more

accurate representation of the electrochemical processes occurring within the system.

Supporting Information

Supporting Information is available from the Wiley Online Library or from the author.

Acknowledgements

T.S.M., S.M.H., and P.R.S. acknowledge support from the UK Engineering and Physical Sciences Research Council (EPSRC) – EP/W03395X/1, EP/X023656/1, EP/W033321/1, EP/P009050/1. Electron Microscopy access was supported by the Henry Royce Institute for Advanced Materials, funded through EPSRC grants EP/R00661X/1, EP/S019367/1, EP/P025021/1 and EP/P025498/1. S.J.H. thanks the European Research Council (ERC) under the European Union's Horizon 2020 research and innovation programme (Grant ERC-2016-STG-EvoluTEM- 715502). X.L. acknowledges funding from the Engineering and Physical Sciences Research Council (EP/X000702/1). The authors acknowledge the European Synchrotron Radiation Facility (ESRF) for the provision of synchrotron radiation facilities under proposal number MI-1484.

Conflict of Interest

The authors declare no conflict of interest.

Author Contributions

J.C. and T.M. conceived the study. J.C., Z.G., Z.Z., and X.Y. prepared the membrane. J.C. and M.P.M. did the spraying coating. J.C. and S.Z. did the fuel cell test. J.C., A.R., B.L., and W.D. did the CT scan. S.J.H. did the FIB-SEM. S.M.H. and P.R.S. advised on the data analysis and result interpretation. J.C. and X.L. did the simulation. J.C. drafted the manuscript and all co-authors reviewed the manuscript.

Data Availability Statement

The data that support the findings of this study are available from the corresponding author upon reasonable request.

Keywords

high-temperature proton exchange membrane fuel cells, HT-PEMFCs, membrane electrode assemblies, multi-physics modelling, visual simulation

Received: November 5, 2024
Revised: March 19, 2025
Published online:

[1] G. Zhang, K. Jiao, *J. Power Sources* **2018**, *391*, 120.
[2] L. Zielke, S. Vierrath, R. Moroni, A. Mondon, R. Zengerle, S. Thiele, *RSC Adv.* **2016**, *6*, 80700.
[3] J. Chen, M. Perez-Page, C. M. A. Parlett, Z. Guo, X. Yang, Z. Zhou, H. Zhai, S. Bartlett, T. S. Miller, S. M. Holmes, *Chem. Eng. J.* **2024**, *487*, 150670.
[4] D. Chen, P. Pei, Y. Li, P. Ren, Y. Meng, X. Song, Z. Wu, *Energy Convers. Manag.* **2022**, *261*, 115651.
[5] Q. Liu, F. Lan, J. Chen, C. Zeng, J. Wang, *J. Power Sources* **2022**, *517*, 230723.
[6] F. A. De Bruijn, V. A. T. Dam, G. J. M. Janssen, *Fuel Cells* **2008**, *8*, 3.
[7] M. Becherif, D. Hissel, S. Gaagat, M. Wack, *J. Power Sources* **2010**, *195*, 6645.
[8] A. Vasilyev, J. Andrews, L. M. Jackson, S. J. Dunnett, B. Davies, *Int. J. Hydrogen Energy* **2017**, *42*, 29406.
[9] S. Ahmad, T. Nawaz, A. Ali, M. F. Orhan, A. Samreen, A. M. Kannan, *Int. J. Hydrogen Energy* **2022**, *47*, 19086.
[10] R. L. Borup, A. Kusoglu, K. C. Neyerlin, R. Mukundan, R. K. Ahluwalia, D. A. Cullen, K. L. More, A. Z. Weber, D. J. Myers, *Curr. Opin. Electrochem.* **2020**, *21*, 192.
[11] Y. Guo, F. Pan, W. Chen, Z. Ding, D. Yang, B. Li, P. Ming, C. Zhang, *Electrochem. Energy Rev.* **2020**, *4*, 67.
[12] A. Parekh, *Front. Energy Res.* **2022**, *10*, 956132.
[13] V. O. Mittal, H. R. Kunz, J. M. Fenton, *J. Electrochem. Soc.* **2007**, *154*, B652.
[14] S. Subianto, M. Pica, M. Casciola, P. Cojocaru, L. Merlo, G. Hards, D. J. Jones, *J. Power Sources* **2013**, *233*, 216.
[15] J. Chen, Z. Guo, M. Perez-Page, Y. Jia, Z. Zhao, S. M. Holmes, *J. Energy Chem.* **2023**, *76*, 448.
[16] J. Chen, M. Perez-Page, Z. Ji, Z. Zhang, Z. Guo, S. Holmes, *J. Power Sources* **2021**, *491*, 229550.
[17] Z. Zhou, Z. Zhao, X. Yang, H. Zhai, L. Ai, J. Chen, S. Holmes, *J. Membr. Sci.* **2024**, *710*, 123135.
[18] L. Zhang, M. Liu, D. Zhu, M. Tang, T. Zhu, C. Gao, F. Huang, L. Xue, *Nat. Commun.* **2024**, *15*, 3409.
[19] Z. Ji, J. Chen, M. Pérez-Page, Z. Guo, Z. Zhao, R. Cai, M. T. P. Rigby, S. J. Haigh, S. M. Holmes, *J. Energy Chem.* **2022**, *68*, 143.
[20] Z. Ji, M. Perez-Page, J. Chen, R. G. Rodriguez, R. Cai, S. J. Haigh, S. M. Holmes, *Energy* **2021**, *226*, 120318.
[21] X. Ren, H. Li, K. Liu, H. Lu, J. Yang, R. He, *Fibers Polym.* **2018**, *19*, 2449.
[22] Z. Guo, J. Chen, J. J. Byun, R. Cai, M. Perez-Page, M. Sahoo, Z. Ji, S. J. Haigh, S. M. Holmes, *J. Energy Chem.* **2021**, *64*, 323.
[23] E. C. S. Transactions, T. E. Society, **2006**, *3*, 931.
[24] T. Romero-Castañón, L. G. Arriaga, U. Cano-Castillo, *J. Power Sources* **2003**, *118*, 179.
[25] G. Mousa, F. Golnaraghi, J. Devaal, A. Young, *J. Power Sources* **2014**, *246*, 110.
[26] J. Lobato, P. Cañ, M. A. Rodrigo, F. J. Pinar, E. Mena, D. U. ´Beda, *Int. J. Hydrogen Energy* **2010**, *35*, 5510.
[27] M. Ercelik, M. S. Ismail, K. J. Hughes, D. B. Ingham, L. Ma, M. Pourkashanian, *Int. J. Hydrogen Energy* **2024**, *50*, 1338.
[28] T. A. M Suter, K. Smith, J. Hack, L. Rasha, Z. Rana, G. A. Ming Angel, P. R. Shearing, T. S. Miller, D. J. L Brett, T. A. M Suter, K. Smith, J. Hack, L. Rasha, Z. Rana, G. M. A Angel, P. R. Shearing, T. S. Miller, D. J. L Brett, *Adv. Energy Mater.* **2021**, *11*, 2101025.
[29] A. E. Khabbazi, A. J. Richards, M. Hoorfar, *J. Power Sources* **2010**, *195*, 8141.
[30] M. Jourdani, H. Mounir, A. Marjani, *Int. J. Multiphys.* **2017**, *11*, 427.
[31] X. Wang, Z. Shi, *Modelling and Simulation*, IntechOpen Limited, UK, **2008**.
[32] D. Gulcin Caglayan, B. Sezgin, Y. Devrim, I. Eroglu, *Int. J. Hydrogen Energy* **2018**, *43*, 10834.
[33] A. D. Shum, D. Y. Parkinson, X. Xiao, A. Z. Weber, O. S. Burheim, I. V. Zenyuk, *Electrochim. Acta* **2017**, *256*, 279.
[34] E. Leonard, A. D. Shum, S. Normile, D. C. Sabarirajan, D. G. Yared, X. Xiao, I. V. Zenyuk, *Electrochim. Acta* **2018**, *276*, 424.
[35] X. Peng, D. Kulkarni, Y. Huang, T. J. Omasta, B. Ng, Y. Zheng, L. Wang, J. M. LaManna, D. S. Hussey, J. R. Varcoe, I. V. Zenyuk, W. E. Mustain, *Nat. Commun.* **2020**, *11*, 3561.

[36] Y. Da Wang, Q. Meyer, K. Tang, J. E. McClure, R. T. White, S. T. Kelly, M. M. Crawford, F. Iacoviello, D. J. L. Brett, P. R. Shearing, P. Mostaghimi, C. Zhao, R. T. Armstrong, *Nat. Commun.* **2023**, *14*, 745.
[37] R. F. Ziesche, J. Hack, L. Rasha, M. Maier, C. Tan, T. M. M. Heenan, H. Markötter, N. Kardjilov, I. Manke, W. Kockelmann, D. J. L. Brett, P. R. Shearing, *Nat. Commun.* **2022**, *13*, 1616.
[38] J. Hack, R. F. Ziesche, M. Fransson, T. Suter, L. Helfen, C. Couture, N. Kardjilov, A. Tengattini, P. Shearing, D. Brett, *J. Phys.: Energy* **2024**, *6*, 025021.
[39] S. H. Eberhardt, M. Toulec, F. Marone, M. Stampanoni, F. N. Büchi, T. J. Schmidt, *J. Electrochem. Soc.* **2015**, *162*, F310.
[40] S. H. Eberhardt, F. Marone, M. Stampanoni, F. N. Büchi, T. J. Schmidt, *J. Synchrotron Radiat.* **2014**, *21*, 1319.
[41] J. J. Bailey, J. Chen, J. Hack, M. Perez-Page, S. M. Holmes, D. J. L. Brett, P. R. Shearing, *J. Power Sources* **2021**, *509*, 230347.
[42] J. Chen, X. Lu, L. Wang, W. Du, H. Guo, M. Rimmer, H. Zhai, Y. Liu, P. R. Shearing, S. J. Haigh, S. M. Holmes, T. S. Miller, *Nat. Commun.* **2024**, *15*, 1.
[43] D. Schonvogel, M. Rastedt, P. Wagner, M. Wark, A. Dyck, *Fuel Cells* **2016**, *16*, 480.
[44] M. Boaventura, A. Mendes, *Int. J. Hydrogen Energy* **2010**, *35*, 11649.
[45] S. Galbiati, A. Baricci, A. Casalegno, G. Carcassola, R. Marchesi, *Int. J. Hydrogen Energy* **2012**, *37*, 14475.
[46] S. Galbiati, A. Baricci, A. Casalegno, R. Marchesi, *Int. J. Hydrogen Energy* **2012**, *37*, 2462.
[47] J. Chen, J. J. Bailey, L. Britnell, M. Perez-Page, M. Sahoo, Z. Zhang, A. Strudwick, J. Hack, Z. Guo, Z. Ji, P. Martin, D. J. L. Brett, P. R. Shearing, S. M. Holmes, *Nano Energy* **2022**, *93*, 106829.
[48] J. Halter, S. Thomas, S. K. Kær, T. J. Schmidt, F. N. Büchi, *J. Power Sources* **2018**, *399*, 151.
[49] H. Becker, L. N. Cleemann, D. Aili, J. O. Jensen, Q. Li, *Electrochem. Commun.* **2017**, *82*, 21.
[50] S. Galbiati, A. Baricci, A. Casalegno, R. Marchesi, *Int. J. Hydrogen Energy* **2013**, *38*, 6469.
[51] B. Sezgin, D. G. Caglayan, Y. Devrim, T. Steenberg, I. Eroglu, *Int. J. Hydrogen Energy* **2016**, *41*, 10001.